JOURNAL OF CATALYSIS 117, 52–70 (1989)

Modeling Wet Impregnation of Nickel on γ-Alumina

P. CHU,[1] E. E. PETERSEN, AND C. J. RADKE[2]

Department of Chemical Engineering, University of California, Berkeley, California 94720

Received March 15, 1988; revised November 1, 1988

A transport model is presented for the coimpregnation of a metal salt and an acid into a porous oxide where equilibrium adsorption is controlled by hydrolysis of surface hydroxyl groups and ion binding on these groups. The transport and adsorption equations for the metal species and the acid are solved simultaneously to determine metal profiles for the wet impregnation of $NiCl_2$ and HCl in a γ-Al_2O_3 support with a background electrolyte of NaCl. For acid pretreatment, the transport and adsorption equations of HCl may be solved alone to establish the pellet pH profile, which is then used as the initial condition for subsequent metal impregnation. An important feature of the equilibrium adsorption model is the generation of protons upon nickel adsorption. As nickel diffuses in and adsorbs, a local excess of H^+ ions is generated, producing a pH profile inside the pellet and reducing nickel uptake. This blocking phenomenon, which cannot be described by Langmuir isotherms, produces unique, concave–convex metal profiles in the pellets. New experimental nickel profiles on γ-Al_2O_3 are determined by electron microprobe analysis over a 0.001 to 0.1 *M* nickel concentration range in 0.1 *M* NaCl aqueous solutions ranging in pH from 5.2 to 7.85. By controlling the initial pH profile through acid pretreatment, the final nickel profile may be modified to produce egg-shell, egg-white, egg-yolk, and uniform catalysts. Comparison of the proposed transport theory and the experimental metal profiles shows good agreement, establishing a new tool for designing oxide support catalysts.

INTRODUCTION

Supported metal catalysts are commonly prepared by metal salt impregnation. In the wet-impregnation method, the prewetted support, usually a porous oxide, is immersed into a liquid solution, typically water, which contains the desired metal as a salt. The dissolved metal species is then carried into the support pellets by diffusion. Conversely, with the incipient-wetness impregnation method, the dry support is immersed in the liquid solution, and the metal salt convects into the pellets by solvent imbibition. For both techniques, the resulting catalysts are then dried, and the catalytic component is activated by calcination and reduction. The impregnation step is the most important in determining the final metal concentration profile, although the last two steps may also affect the profile to a lesser extent.

The metal loading profile of the supported catalyst is an important factor in determining the performance of the catalyst (*1–3*). Figure 1 shows the four major types of profiles. Because adsorption of metal ions from aqueous solution is strongly dependent on pH, the acidity of the impregnating solution is known to be an important factor in determining the final profile. Numerous studies have shown experimentally how acids and salts can affect the metal profile of the catalysts (*4–8*). Modeling of impregnation profiles has also been attempted by several investigators with varying degrees of success (*7–10*). The main stumbling block appears to be the oversimplified surface chemistry. Most researchers employ a Langmuir, site-competition adsorption model to describe the effect of solution pH on metal uptake. However, the Langmuir model cannot describe the equilibrium adsorption of acid or base, as evi-

[1] Currently with Geomatrix Consultants, San Francisco, CA.

[2] To whom correspondence should be addressed.

0021-9517/89 $3.00

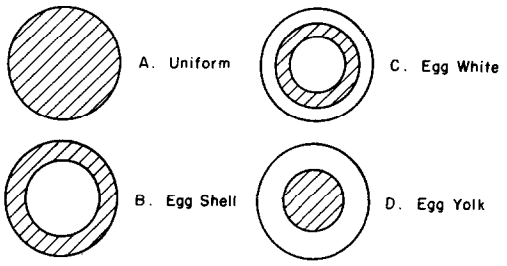

FIG. 1. The four major types of metal profiles in supported catalysts.

denced by the inability to obtain constant parameters that are valid over a wide range of pH and salt concentration.

Although incipient-wetness methods are more commonly employed industrially, we focus here on wet impregnation because it is easier to model and because it reveals the importance of the underlying surface chemistry with greater sensitivity. Extension to the incipient-wetness system does not appear to be a major step. The advantage of wet impregnation is therefore to provide a discriminating test of the oxide/aqueous solution interface chemistry.

Accordingly, in this research, we incorporate a realistic portrayal of ion exchange on oxide surfaces into the transport modeling of wet impregnation. The Davis, James, and Leckie (DJL) picture of the oxide/aqueous interface is shown in Fig. 2 (*11*). Vicinal hydroxyl groups, SOH, terminate the oxide lattice. In response to solution pH these surface sites hydrolyze, leading to a surface charge and a concomitant surface potential:

$$SOH + H^+ \rightleftarrows SOH_2^+, \quad (1)$$

$$SOH + OH^- \rightleftarrows SO^- + H_2O. \quad (2)$$

All ionic species in solution may compete in ion-binding reactions for the surface hydroxyl groups on the oxide support. Of particular importance in this work is the complexing reaction of dissolved nickel (*12*)

$$Ni^{2+} + H_2O + SOH \rightleftarrows SO^-NiOH^+ + 2H^+, \quad (3)$$

which generates two protons for every metal ion adsorbed. Adsorption of an ion depends not only on its solution concentration, but also on the surface charge of the oxide, which is in turn a strong function of pH. Equation (3) explains the origin of the depression of nickel adsorption uptake under acidic conditions, and it indicates why a Langmuir description fails. Additional details on the DJL triple-layer electrostatic model are available in Appendix A and in the original article (*11*).

Lewnard (*12*) has measured batch adsorption of HCl and $NiCl_2$ on powdered γ-alumina at various NaCl concentrations and has applied the DJL equilibrium model using the numerical scheme of Westall (*13*). One consistent set of parameters successfully fits the experimental results over a wide range of NaCl and $NiCl_2$ concentra-

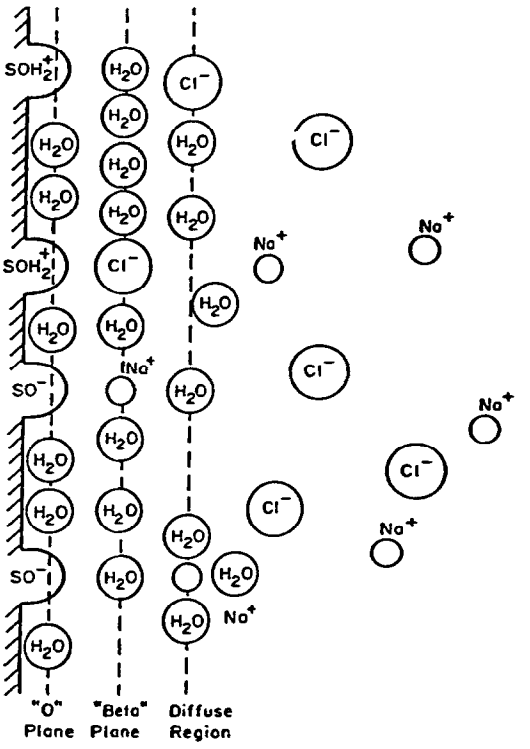

FIG. 2. Schematic of hydrolysis and ion-complexing of surface hydroxyl groups at the aqueous/oxide interface according to the triple-layer electrostatic model of Davis *et al.* (*11*).

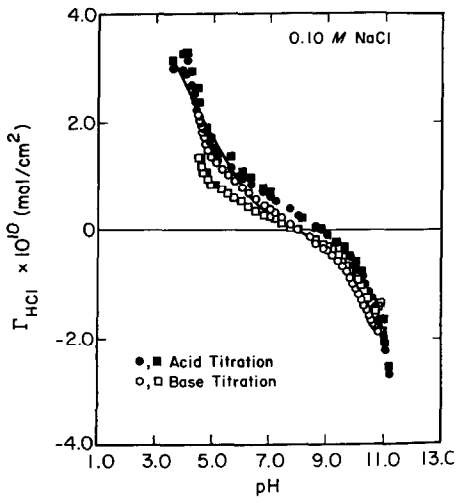

FIG. 3. Acid adsorption on γ-alumina in 0.1 *M* NaCl. Closed and open symbols refer to titration in the acid (HCl) and base (NaOH) directions, respectively. pH 7.85 is the point of zero charge. The solid line is a best fit to the triple-layer electrostatic model as outlined in Appendix A.

tions and pH. These are listed in Appendix A. Figures 3 and 4 report the acid and nickel isotherms in 0.1 *M* NaCl, where the solid lines in these figures correspond to the adsorption predicted by the DJL electrostatic triple-layer model. Positive values of Γ_{HCl} in Fig. 3 reflect a cationic surface charge, whereas negative values correspond to an anionic surface charge. The surface is electrically neutral at the point of zero charge of pH 7.85. The strong blocking action of acid on nickel adsorption is seen in Fig. 4. Nickel uptake is diminished by more than an order of magnitude when the pH is lowered from 7 to 5. Nickel and acid adsorption isotherms at other background salt concentrations as well as isotherms for sodium and chloride ions are available in Lewnard's thesis (*12*).

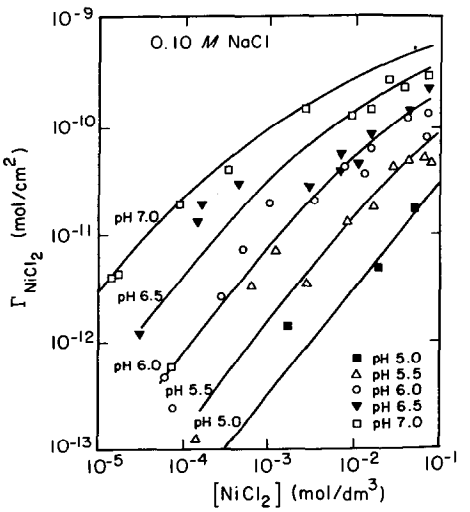

FIG. 4. Nickel adsorption on γ-alumina in 0.1 *M* NaCl for various pH solutions. The solid lines are best fits to the triple-layer electrostatic model as outlined in Appendix A.

Our goal is to incorporate the DJL equilibrium, triple-layer model into a transport formulation for wet impregnation of oxide support pellets. The theory section below presents the requisite, coupled diffusion equations and illustrates the importance of the pretreatment pH profile of the pellet in controlling the final metal profile. New, experimental radial profiles are reported next for nickel in cylindrical γ-alumina pellets, as determined by electron microprobe analysis. By careful control of pH, egg-shell, egg-white, egg-yolk, or uniform profiles can be produced. Comparison of theoretical and experimental profiles and discussion constitute the final sections. Because of the unique feature of proton generation upon nickel adsorption exhibited in Eq. (3), we find good agreement between the experimental and theoretical nickel profiles using only predetermined equilibrium adsorption parameters.

TRANSPORT FORMULATION

Conservation Equations

The continuity equation for dilute ionic species in an adsorptive porous medium is well known (*14, 15*). It is written here for the species H^+, OH^-, and a divalent metal cation, M^{2+}, and averaged over a representative volume element of the porous pellet. For the transport of hydrogen and hydroxyl ions, a reaction term accounting for water dissociation must be included in the formu-

lation (*12, 14*). When this term is eliminated algebraically, we recover the following conservation statements for diffusion of H^+, OH^-, and M^{2+} in an adsorptive porous solid (*12*):

$$\frac{\partial([H^+] - [OH^-])}{\partial t} + \frac{(1-\phi)\,A_v}{\phi}\frac{\partial(\Gamma_{H^+} - \Gamma_{OH^-})}{\partial t} = \frac{D_{H^+}}{\theta^2}\nabla^2[H^+] - \frac{D_{OH^-}}{\theta^2}\nabla^2[OH^-], \quad (4)$$

$$\frac{\partial[M^{2+}]}{\partial t} + \frac{(1-\phi)A_v}{\phi}\frac{\partial\Gamma_{M^{2+}}}{\partial t} = \frac{D_{M^{2+}}}{\phi^2}\nabla^2[M^{2+}]. \quad (5)$$

Here, ϕ is the pellet porosity, θ is the tortuosity of the pellet, A_v is the surface area per unit solid volume, and Γ_i is the adsorption of species i in all molecular forms per unit solid surface area. All other symbols have their usual meanings. Convection is neglected since diffusion is the primary means of transport in wet impregnation. Likewise, electrical field migration may be neglected because the concentration of the background electrolyte, NaCl, is much greater than the species of concern (*15*). In this study, the metal aqueous species is taken to be only an uncomplexed divalent cation. Multivalent cations hydrolyze in aqueous solution, but in the range of pH studied here, the dominant species is Ni^{2+} (*12*). Equation (4) is written in terms of the difference in concentrations of H^+ and OH^-. Thus, a change in local pH may be caused by movement of H^+ in one direction, or movement of OH^- in the opposite direction, or a combination of both fluxes. Written in this manner, Eq. (4) is valid over the entire range of pH without a discontinuity at neutral pH (*14*).

The transport equations involve the solution phase species concentrations. Thermodynamic components need to be defined in terms of the solution species. If Cl^- is the anion of the background electrolyte, the acid, and the metal salt, then the solution components are HCl and MCl_2 (*12*). The concentrations of these components are defined in terms of the solution species as

$$C_{HCl} \equiv C_1 = [H^+] - [OH^-], \quad (6)$$

$$C_{MCl_2} \equiv C_2 = [M^{2+}]. \quad (7)$$

With this definition, C_{HCl} may be positive or negative depending on the pH.

Similarly, component adsorption is defined in terms of the species adsorption, as discussed by Lewnard (*12*):

$$\Gamma_{HCl} \equiv \Gamma_1 = \Gamma_{H^+} - \Gamma_{OH^-}, \quad (8)$$

$$\Gamma_{MCl_2} \equiv \Gamma_2 = \Gamma_{M^{2+}}. \quad (9)$$

Here the species adsorption incorporates all possible molecular forms, and includes ions complexed at the surface and those located in the diffuse layer [see Appendix A and Refs. (*11, 12*)]. Note in Appendix A that Γ_{HCl} does account for the two protons released for every nickel ion adsorbed following Eq. (3). The adsorption of HCl may be positive or negative, depending on the pH (cf. Fig. 3).

The conservation equations are nondimensionalized as follows. Let C_{10}° be the initial acid concentration at the pellet center and let C_{10}^{∞} be the initial acid concentration in the bulk external solution. The corresponding metal concentrations are written as C_{20}° and C_{20}^{∞}. Then, the dimensionless acid and metal component concentrations become

$$\tilde{C}_1 \equiv \frac{C_1 - C_{10}^{\circ}}{C_{10}^{\infty} - C_{10}^{\circ}}, \quad (10)$$

$$\tilde{C}_2 \equiv \frac{C_2 - C_{20}^{\circ}}{C_{20}^{\infty} - C_{20}^{\circ}}. \quad (11)$$

Since the adsorption of HCl and that of $NiCl_2$ may be different by orders of magnitude (compare Figs. 3 and 4), the adsorption of each must be scaled separately. We use the maximum values possible under a given set of initial conditions, denoted as $\Gamma_{1,max}$ and $\Gamma_{2,max}$, respectively:

$$\tilde{\Gamma}_1 = \frac{\Gamma_1}{\Gamma_{1,\max}}, \quad (12)$$

$$\tilde{\Gamma}_2 = \frac{\Gamma_2}{\Gamma_{2,\max}}. \quad (13)$$

To follow the movement of the metal, time is nondimensionalized with the diffusion coefficient of hydrogen ions, and the maximum adsorption and the concentration of the metal species:

$$\tau = \frac{D_{H^+} t}{\theta^2 R^2} \frac{\phi}{(1-\phi)A_v} \frac{(C_{20}^{\infty} - C_{20}^{\circ})}{\Gamma_{2,\max}}. \quad (14)$$

R is the radius of the cylindrical pellets which are taken here to be infinitely long. Accordingly, the gradient and Laplacian operators refer in this work to the radial direction in a cylindrical geometry. The symbol ζ later denotes the dimensionless pellet radius, $\zeta = r/R$. Because the surface area of typical porous supports is very large, adsorption loading dominates the pore solution concentration. This dictates scaling time by a measure of the isotherm chord. Using the characteristic metal isotherm chord proves convenient since we are interested primarily in tracking metal profiles.

By invoking local equilibrium for water dissociation, the concentrations of hydrogen and hydroxyl ions may be eliminated in favor of $\tilde{C}_1$. After considerable algebra, the final forms of the transport equations reduce to

$$\frac{1}{\beta}\frac{\partial \tilde{C}_1}{\partial \tau} + \alpha \frac{\partial \tilde{\Gamma}_1}{\partial \tau} = \left(1 - \tfrac{1}{2}(1 - \tilde{D}_1)\left[1 - \frac{\gamma + \tilde{C}_1}{(2K + [\gamma + \tilde{C}_1]^2)^{1/2}}\right]\right) \nabla^2 \tilde{C}_1 + \left(\frac{K(1-\tilde{D}_1)}{(2K + [\gamma + \tilde{C}_1]^2)^{3/2}}\right) (\nabla \tilde{C}_1)^2, \quad (15)$$

$$\frac{1}{\beta}\frac{\partial \tilde{C}_2}{\partial \tau} + \frac{\partial \tilde{\Gamma}_2}{\partial \tau} = \tilde{D}_2 \nabla^2 \tilde{C}_2, \quad (16)$$

where the gradient operator is now in dimensionless form. The square gradient term $(\Delta \tilde{C}_1)^2$ arises when $[OH^-]$ is eliminated using the water dissociation equilibrium (14). Dimensionless parameters in Eqs. (15) and (16) are defined as $K \equiv 2K_w/(C_{10}^{\infty} - C_{10}^{\circ})^2$, $\gamma \equiv C_{10}^{\circ}/(C_{10}^{\infty} - C_{10}^{\circ})$, $\tilde{D}_1 \equiv D_{OH^-}/D_{H^+}$, $\tilde{D}_2 \equiv D_{M^{2+}}/D_{H^+}$,

$$\alpha \equiv \frac{\Gamma_{1,\max}}{(C_{10}^{\infty} - C_{10}^{\circ})} \frac{(C_{20}^{\infty} - C_{20}^{\circ})}{\Gamma_{2,\max}}, \quad (17)$$

$$\beta \equiv \frac{(1-\phi)A_v}{\phi} \frac{\Gamma_{2,\max}}{(C_{20}^{\infty} - C_{20}^{\circ})}. \quad (18)$$

The parameter α is the ratio of the characteristic isotherm chords for the acid and the metal, and β is a dimensionless metal isotherm chord reflecting the relative partitioning of the metal between the oxide surface and the pore solution.

If metal is impregnated into a pellet whose initial pore and bulk acid solution concentrations are identical so that $C_{10}^{\circ} = C_{10}^{\infty}$, then $\tilde{C}_1$ must be scaled with the initial bulk solution concentration, viz., $\tilde{C}_1 = C_1/C_{10}^{\infty}$. In this case, C_{10}° is formally set to zero in all relevant nondimensional parameters. Equation (15) is no longer valid. Fortunately, its correct form emerges simply in the limit of γ approaching zero.

Equations (15) and (16) are highly nonlinear and strongly coupled through the intricate adsorption equilibria of the DJL model, as described in Appendix A. In particular, because of Eq. (3), the adsorption of nickel essentially is inversely proportional to the square of the concentration of H^+ and directly proportional to the concentration of the metal.

Diffusion is several orders of magnitude slower than ion-exchange adsorption kinetics (*16–19*), so we assert that the surface is in equilibrium with local pore concentrations of HCl and MCl_2. Tsai (*20*) has reported that desorption of nickel from γ-alumina is much slower than adsorption. Since our transport model invokes local equilibrium, metal ion desorption may be falsely predicted. However, the conditions of our experiments are such that adsorption of nickel continually increases, and no desorption occurs.

One very important assumption is that

the concentration of the background electrolyte, NaCl, is large compared to the concentrations of HCl and $NiCl_2$ and remains constant throughout the pellet. Any changes in adsorption of Na^+ and Cl^- are assumed to be small, affecting the pore solution concentration of NaCl very little. The large constant concentration of NaCl maintains electroneutrality in the pore solution and permits the electrical migration of ions to be neglected (*15*).

Equation (15) must be modified to calculate the pellet pH profile during acid pretreatment when no nickel is present in solution. Time is now nondimensionalized by the maximum adsorption and the concentration of HCl instead of the metal species, and the dimensionless ratio β contains the maximum adsorption and the concentrations of HCl. The α factor becomes unity.

Initial conditions for Eqs. (15) and (16) are concentrations at the edge of the pellet, $\tilde{C}_1(1, 0)$ and $\tilde{C}_2(1, 0)$, equal to one, and pore solution concentrations throughout the pellet, $\tilde{C}_1(\zeta, 0)$ and $\tilde{C}_2(\zeta, 0)$, equal to zero. Boundary conditions include radial symmetry for both components, and that solution concentrations of metal and acid at the pellet radius remain equal to the corresponding bulk solution concentrations. The concentrations of HCl and MCl_2 in the bulk solution remain constant as the solution volume to total surface area of pellets is set to be large.

For the case of acid pretreatment, the nonuniform pH profile is calculated from Eq. (15) suitably modified as enunciated above. This calculated pH profile then serves as the initial condition for the subsequent metal impregnation.

Eight nonlinear, coupled equations are solved simultaneously: two transport equations for HCl and $NiCl_2$ [Eqs. (15) and (16)], two equations defining adsorption of HCl and $NiCl_2$ [Eqs. (A16) and (A17)], and four equations pertinent to the adsorption equilibria [Eqs. (A12)–(A15)], as described in Appendix A. The variables solved are $\tilde{C}_1$, $\tilde{C}_2$, $\tilde{\Gamma}_1$, $\tilde{\Gamma}_2$, the fraction of empty surface hydroxyl sites, and the exponentials of the negative nondimensional electrostatic potentials, $-\Psi_i$, at the three surface planes of the DJL model (see Appendix A and Fig. 2). Galerkin's numerical method of finite elements was employed with linear basis functions and with a scaled Newton's procedure to iterate the nonlinearities. A simple backward Euler scheme tracked the time evolution. Because radial profiles of several of the variables are very steep, approaching step functions, up to 100 elements were required; most of these were placed near the pellet exterior. Initially, when the profiles were steepest, dimensionless time increments down to 10^{-4} were demanded. Chu (*21*) gives considerable more detail on the numerical procedures.

As indicated in the theoretical calculations reported below, excess protons generated by metal ion adsorption create unique concave–convex metal profiles. The theoretical calculations also illustrate how dramatically the pretreatment acid profile in the pellet influences the metal loading profile in the catalyst support. Specifically, the depth of initial acid penetration, because of acid blocking of nickel uptake, determines the location of the nickel band in an egg-white or egg-yolk catalyst.

Theoretical Profiles

The sample calculations presented in this section illustrate how the transport model can predict egg-shell, egg-white, egg-yolk, and uniform catalysts upon wet impregnation. Equilibrium sorption parameters are taken from Lewnard's experimental work (*12, 14*) and are noted in Appendix A. Diffusion coefficients of each ion are those at infinite dilution in water at 25°C (*15*): $D_{H^+} = 9.3 \times 10^{-5}$, $D_{OH^-} = 5.3 \times 10^{-5}$, and $D_{Ni^{2+}} = 7.0 \times 10^{-6}$ all in cm^2/s. Physical properties of the γ-alumina pellet are given in the experimental section. No measurements were made of the tortuosity, but Satterfield recommends a value of $\theta^2 = 4$ (*22*).

Figure 5 illustrates the metal concentration profiles for 0.05 *M* $NiCl_2$ in 0.1 *M* NaCl

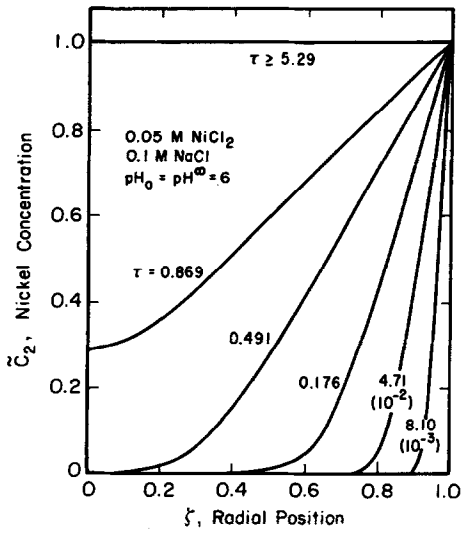

FIG. 5. Calculated nickel concentration profiles in a cylindrical pellet, whose initial pH is uniform at 6, immersed in a bath of pH 6 and 0.05 *M* nickel. Requisite parameters are $\Gamma_{1,max}$ (pH 6, $[Ni^{2+}] = 0.05\ M$) $= -1.17 \times 10^{-10}$ mol/cm^2, $\Gamma_{2,max}$ (pH 6, $[Ni^{2+}] = 0.05\ M$) $= 1.34 \times 10^{-10}$ mol/cm^2, $\tilde{D}_1 = 0.57$, $\tilde{D}_2 = 7.5 \times 10^{-2}$, $K = 2.0 \times 10^{-2}$, $\alpha = -4.45 \times 10^4$, $\beta = 9.48$, $\gamma \equiv 0$.

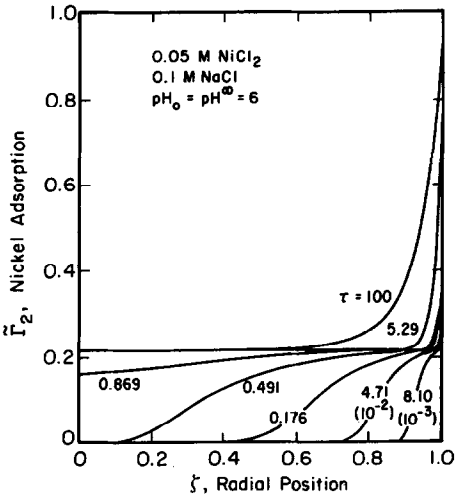

FIG. 6. Calculated nickel adsorption profiles in a cylindrical pellet, whose initial pH is uniform at 6, immersed in a bath of pH 6 and 0.05 *M* nickel. Parameters are those of Fig. 5.

diffusing into a cylindrical γ-alumina pellet. The initial pH of the interior of the pellet and the bulk solution is 6.0; the bulk concentration of $NiCl_2$ and the bulk solution pH are fixed constant in time. Under these conditions, Figs. 3 and 4 reveal that acid adsorption and nickel adsorption are about the same even though the nickel concentration is a factor of 10^4 larger. The pore-solution, radial concentration profiles of nickel in Fig. 5 show expected diffusion behavior with a uniform concentration emerging after $\tau \geq 5$.

Figure 6 shows the corresponding concave–convex adsorption profiles of nickel. It is important to realize that the surface area-to-volume ratio, A_v, is very large (i.e., β is large). The amount of nickel on the surface, although it may occupy only a small percentage of the available adsorption sites, is much larger than the amount of nickel in the adjacent pore solution. Thus, the total amount of nickel measured by microprobe profiling is essentially the amount of nickel adsorbed. According to Fig. 6, theory is this case predicts an egg-shell metal profile. Finally, Fig. 7 displays the pellet pH profiles.

The behavior in Figs. 5–7 can be explained as follows. As nickel diffuses into the pellet and adsorbs, excess H^+ ions are released [cf. Eq. (3)], causing the local pH just inside the pellet exterior to drop from its initial value of 6 to about 5.4. Since the

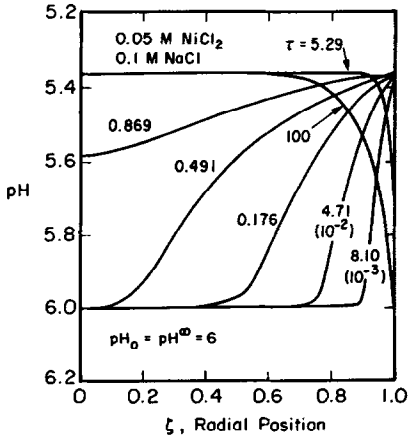

FIG. 7. Calculated pH profiles in a cylindrical pellet, whose initial pH is uniform at 6, immersed in a bath of pH 6 and 0.05 *M* nickel. Parameters are those of Fig. 5.

pH has decreased, acid adsorption increases while adsorption of nickel is inhibited in that region, as illustrated in Fig. 6. Relative to characteristic diffusion times, all these adjustments are made essentially instantaneously to achieve equilibrium. Because of the reduced adsorption of nickel ions, they diffuse past the region of low pH and move farther into the pellet to a region of higher pH. Here they again adsorb and lower the pH in that region. Basically, the diffusing nickel carries with it a pH wave. The nickel continues to diffuse in and adsorb in this manner until, after several time constants, the concentration of nickel in the center and throughout the pellet is equal to that of the bulk. At this juncture, however, the pellet pH is more acidic than the bulk.

Since the pH at the pellet exterior remains constant at 6, the adsorption of nickel at the pellet exterior surface is higher than in the lower pH interior. This produces a rather uniform nickel profile with a sharp increase in loading at the pellet exterior (i.e., an egg shell). The uniform interior loading may be termed a pseudo-steady state because the nickel profile changes very slowly after it has reached this point. The reason is that migration of the H^+ ions is much slower relative to the metal ions because of the smaller concentration gradient and the much larger isotherm adsorption chord for the acid. Thus, the excess H^+ ions generated in the pellet interior do not move much within the time it takes for the concentration of nickel to reach the pseudo-steady state.

Figure 7 shows that after about one nickel adsorption time constant, the pH of the interior is approaching the pseudo-steady-state value of 5.36. Meanwhile, the excess H^+ ions produced by the nickel adsorption diffuse very slowly out to the exterior solution (i.e., the pH exactly at the pellet edge remains at 6; however, this is difficult to see in Fig. 7 at early times because the profiles are very steep). As the pH near the pellet edge slowly rises to 6, adsorption of nickel increases, maintaining local equilibrium with the bulk acid and nickel concentrations. Note in Figs. 6 and 7 that even after 100 time constants, acid is only beginning to exit the pellet in significant amounts. Eventually, the nickel and acid will reach equilibrium with the bulk exterior solution, and the nickel profile will be uniform throughout the pellet at the value of unity in Fig. 6.

The pH in the pellet interior at the pseudo-steady state may readily be calculated by performing a simple mass balance on HCl,

$$\phi C_{10} + (1 - \phi)A_v\Gamma_{10} = \phi C_{1s} + (1 - \phi)A_v\Gamma_{1s},$$

where C_{10} and Γ_{10} represent the concentration and adsorption of HCl before any nickel has diffused in, and C_{1s} and Γ_{1s} represent the concentration and adsorption of HCl after nickel has reached the pseudo-steady state, characterized by the bulk concentration of nickel. C_{10} and Γ_{10} are known from the initial conditions, and C_2 is equal to the bulk solution nickel concentration, C_2^∞. Γ_{1s} is coupled to C_{1s} and C_2^∞ through the adsorption equilibria of Appendix A.

Results of the type in Figs. 5–7 could not have been predicted with a simple, competitive adsorption isotherm. For example, the traditional Langmuir isotherm cannot describe creation of protons upon metal adsorption and, therefore, cannot predict the nickel profiles seen in Fig. 6.

To produce a uniform profile without the sharp increase at the pellet exterior surface, the pH of the bulk solution should be lowered to the pH of the interior of the pellet attained at the pseudo-steady state. The proposed transport theory then predicts that nickel adsorption is repressed at the pellet surface because of the lowered bulk solution pH, resulting in a uniform profile at later times (*21*). Of course, at early times ($\tau \ll 1$), an egg-shell type catalyst is still produced.

Finally, to create an egg-yolk or egg-white catalyst, the pH profile of the pellet must be nonuniform prior to nickel impreg-

nation such that the exterior layer of the pellet is at a lower pH than the pellet core (*21*). Nickel ions will then diffuse relatively quickly past the lower pH shell and deposit nearer to the pellet center, creating an egg-white profile. As nickel diffusion continues, the egg-white profile merges to produce an egg-yolk catalyst.

Based on the theoretical calculations, we assert that metal profiles for wet impregnation can be tailored by judicious choice of pH conditioning of the support pellets. This assertion is now tested experimentally.

EXPERIMENTAL

Nickel-on-Al_2O_3 supports were prepared by wet impregnation. The γ-Al_2O_3 pellets (W. R. Grace) are in the form of extruded cylinders, 0.32 cm in diameter and with length-to-diameter ratios widely spread about unity. The N_2 BET specific surface area is 270 m^2/g, and the volume-average pore throat radius is 5.5 nm, as determined from mercury porosimetry. The bulk density of the particles is 0.934 g/cm^3, giving a surface area-to-solid volume ratio of A_v = 9.2×10^6 cm^2/cm^3. Pellet porosity is ϕ = 0.723.

A baffled tank, stirred by four, nylon-mesh cylindrical baskets arranged in a square pattern, was used for the acid and nickel impregnation experiments (*12, 14*). Experiments were carried out at ambient temperature, 23°C, and a N_2 blanket excluded CO_2 from the stirred tank. Prior to each experiment, support pellets were dried in a desiccator containing anhydrous $CaSO_4$ (Drierite) for at least 12 h under house vacuum (approximately 5 psi) after nonuniformly shaped and broken or cracked pellets had been sorted by hand and removed. Approximately 9 to 12 g of the dried pellets was then placed in the baskets and immersed in the stirred tank containing 1.0 to 1.4 liters of distilled, deionized water (Barnstead distilled and polished with a Milli-Q water purification system) at 0.1 *M* NaCl. Analytical-grade HCl or NaOH was used to adjust the initial pH of the solution. For acid pretreatment, the pellets were immersed in the bath for a specified length of time, typically 3 to 5 days. For some experiments, the bath was kept at a constant pH using an automatic titrator (Metrohm Titrator E 526 and a Metrohm 655 Dosimat). If the pellets were just to be prewet, they were assumed to be filled with solution when bubbles stopped rising from them, approximately 1.5 min. The pellets were then kept in solution for one more minute before further treatment.

After the pellets had been filled with the initial solution or treated with acid, they were impregnated with nickel. Again, approximately 1.0 to 1.4 liters of solution was used for each experiment, consisting of $NiCl_2$ and 0.1 *M* NaCl dissolved in the distilled, deionized water. HCl or NaOH was used to adjust the pH of the solution. The pH was monitored and for certain impregnation experiments, the bath was kept at a constant pH with the automatic titration setup.

No more than four samples of the catalyst pellets were taken during each experiment, and each sample was approximately one-fourth of the total amount of pellets used in the experiment. The samples were freeze-dried with liquid nitrogen to repress movement of the nickel profile during drying. The dried pellets were calcined at 300°C for 2 h with flowing air, reduced with an equimolar mixture of flowing H_2 and N_2 at 300°C for 3 to 5 h, and then cooled under flowing nitrogen to prevent reoxidation of the metal.

To prepare the pellets for microprobe analysis, 5 to 10 pellets from each sample were submerged in a Spurr, 60-mPa · s embedding medium (PolySciences, Inc.) under house vacuum so that the resin penetrated through the pores into the center of the pellets. To obtain a cross section of the pellets, the top half of the cured probe sample was carefully ground using silicon carbide grinding paper (240 grit) with water as a lubricant. The samples were then placed in an automated polisher (Mico Instruments,

Inc., No. 137) for 40 to 60 min using 3-μm diamond paste and mineral oil. Final polishing stages were performed by hand using, respectively, 0.25- and 0.01-μm diamond paste and mineral oil. An even layer of evaporated carbon, approximately 25 nm thick, was then coated onto the samples.

An ARL SEMQ wavelength-dispersive electron microprobe was used for quantitative elemental analysis of aluminum, oxygen, nickel, sodium, and chlorine. Points were taken about 10 to 50 μm apart along the diameter of each pellet. Since the surface of the pellet is not smooth on a microscopic level, the electron beam was diffused to a 15-μm beam spot size to obtain meaningful average X-ray intensities.

A clean γ-alumina pellet, which had been previously wet with the 0.1 *M* NaCl solution, freeze-dried, calcined, and reduced, was used as a calibration standard for the aluminum and oxygen and as a background for nickel analyses. A calibration standard of pure nickel metal was used for nickel analysis. Since the actual concentration of nickel in the sample pellets is small, the correction factors, necessary for quantitative probe analysis (*23, 24*) for each of the elements, are based primarily on the aluminum and oxygen concentrations. These concentrations are automatically corrected for the porous nature of the samples by using the nascent Al_2O_3 support as the calibration standard for aluminum and oxygen. Any contribution to the correction factors based on the nickel content is very small, so adopting a homogeneous metal standard for nickel analysis introduces little error.

To establish reproducibility, nickel profiles for two or three pellets from each sample were measured with the microprobe. All profiles from the same sample agreed well with each other with a difference of at most 10% occurring only for the smallest nickel loadings (*21*). This finding also indicates a minimal effect of diffusion influx from the ends of the cylindrical pellets, justifying the one-dimensional theoretical transport analysis.

Probe analysis of a clean pellet which was prewet with the NaCl solution, freeze-dried, calcined, and reduced showed no nickel present (≤0.01 wt%), and the aluminum/oxygen molar ratios were approximately 2 to 3 in agreement with the alumina stoichiometry. Considerable more detail on the experimental procedures is available elsewhere (*21*).

In all the experiments performed in this study, the final concentration of nickel in the external bath was always at least 90% of the initial concentration. Lewnard has also shown that any external mass-transfer effects are only important for short times (*12*). Thus, for all of the calculations reported under Results, the solution concentration of nickel in the bulk and at the exterior of the pellet are assumed to remain constant and equal throughout each experiment.

RESULTS

We report new experimental profiles of nickel on γ-alumina of the egg-shell, egg-white, and egg-yolk types. Numerous additional profile data may be found in the thesis of Chu (*21*). Parameters for the companion theory calculations are set a priori at the values listed in the theory and experimental sections, except that the diffusivity of hydrogen ions was raised to 2.7×10^{-4} cm^2/s (alternately, the pellet tortuosity could have been lowered).

Egg-Shell Profiles

For the egg-shell profiles, dry pellets were immersed in a solution of 0.1 *M* NaCl at a pH of 7.85 corresponding to the point of zero charge for 2.5 min to fill the pores with solution. They were then immersed in a solution of 0.001 *M* $NiCl_2$ and 0.1 *M* NaCl, pH 7.85. The automatic titration setup maintained a constant pH in the bulk solution. Samples were taken after 4, 48, 69, and 168 h, and the respective nickel profiles in weight percent are displayed as open symbols in Figs. 8–11. The nondimensional linear coordinate across the pellet diameter

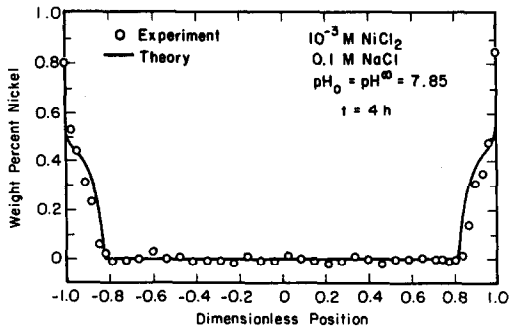

FIG. 8. Nickel profile in a γ-alumina pellet after 4 h. Initially the pellet has a uniform pH of 7.85, and is then immersed into a bath of pH 7.85 and 10^{-3} M nickel. Requisite parameters are $\Gamma_{1,max}$ (pH 7.85, $[Ni^{2+}] = 10^{-3}$ M) $= -5.03 \times 10^{-10}$ mol/cm^2, $\Gamma_{2,max}$ (pH 7.85, $[Ni^{2+}] = 10^{-3}$ M) $= 3.08 \times 10^{-10}$ mol/cm^2, $\bar{D}_1 = 0.20$, $\bar{D}_2 = 2.6 \times 10^{-2}$, $K = 4.15 \times 10^{-2}$, $\alpha = 2.36 \times 10^3$, $\beta = 1.08 \times 10^3$, $\gamma \equiv 0$.

ranges from -1 (left outside edge) to $+1$ (right outside edge). Note the excellent symmetry of the experimental profiles, lending confidence to our results.

To calculate theoretically these nickel profiles, the initial pH profile must be known. As the aqueous solution imbibes into the dry pellets, H^+ and OH^- ions hydrolyze the surface hydroxyl groups. Since at the point of zero charge, equal amounts of H^+ and OH^- are taken up, the pH of the pore solution must remain constant during acid (or base) imbibition into the pellet. Thus, the pH profile after the solution has filled the pores is uniform with a value of 7.85 (cf. Fig. 3). This is the initial condition from which the theoretical calculations proceed.

In all nickel profiles reported in Figs. 8–11, the very highest points of the experimental and theoretical curves at the outside edges of the pellets are not displayed to allow magnification of the scale. The theoretical curve is very steep at the outside edges and rises to a predicted nickel weight percent of 4.90. The measured nickel content never quite attains this level. This may be explained by lack of uniform exposure of some pellets stacked in the nylon baskets to the well-mixed bulk solution and by the inability to focus the 15-μm microprobe beam directly at the pellet edges (*21*).

Figures 8 and 9 show the radial nickel profiles of a pellet from the first and second samples taken at 4 and 48 h. The theoretical (solid lines) and experimental (open symbols) profiles agree very well. The microprobe data confirm the steep gradients near the pellet exterior surface and the convex shape of the nickel profile as it moves in. Indeed Figs. 8–11 all reflect the predicted shapes of Fig. 6. The location of the nickel front is correctly predicted. As explained in the theoretical section, the nickel profile is convex in shape because of the protons generated upon nickel adsorption. Due to strong adsorption partitioning, these excess protons inside the pellet cannot readily diffuse outward so that nickel adsorption is inhibited relative to that at the exterior surface (cf. Figs. 6 and 7). At the pellet edge, the excess protons do diffuse out to match the bulk pH of 7.85, keeping nickel adsorption there high. Again, such concave–convex profile shapes would not be seen using a simple, site-competition adsorption model.

Figures 10 and 11 show pellet profiles from the third sample taken after 69 h and the fourth sample taken after 168 h. The convex nickel wave is again clearly shown with center overlap just commencing in Fig. 11. The theoretical profiles, however, demand that the nickel move farther into

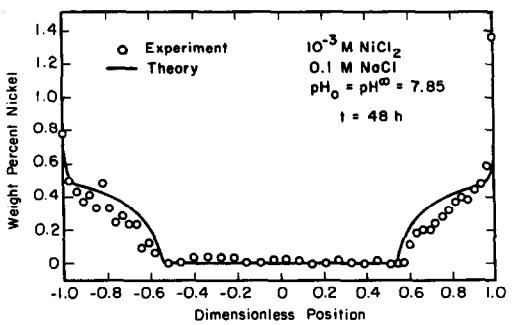

FIG. 9. Nickel profile in a γ-alumina pellet after 48 h. Conditions and parameters are those of Fig. 8.

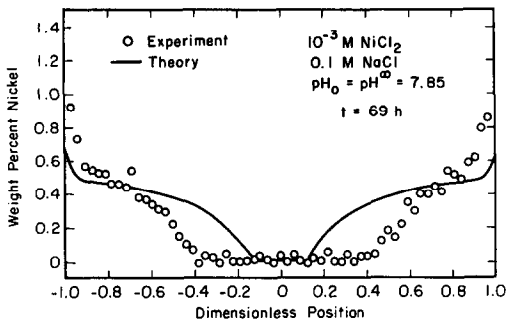

FIG. 10. Nickel profile in a γ-alumina pellet after 69 h. Conditions and parameters are those in Fig. 8.

the pellet than the probe data show. Indeed, theory predicts the pseudo-steady-state nickel profile mentioned above after 168 h, yet the experimental profile lags behind. Theory also indicates a sharp concave profile just inside the pellet while the probe data show a more gradual decrease of nickel adsorption. In both Figs. 10 and 11, the experiments reveal more nickel just under the exterior surface of the pellet. This increased metal adsorption region slows diffusion into the pellet interior, which is consistent with the nickel front not penetrating as far into the pellet as predicted by theory.

Egg-White and Egg-Yolk Profiles

Based on the reasoning put forth in the theory section, the next set of experiments consisted of acid pretreatment to yield a pellet with a region of lower pH at the pellet exterior relative to the interior, followed by nickel impregnation at the lower pH. The pH profile during the acid pretreatment step is calculated from theory and is used as the initial condition for the nickel profile prediction.

For the acid pretreatment, the pellets were prewet with a solution of 0.1 *M* NaCl at the point of zero charge, pH 7.85, as above. They were then immersed into a solution of 0.1 *M* NaCl at pH 5.2. The pH of the bulk solution was kept constant by automatic titration for 5 days. The pellets were taken from the pretreatment solution and immersed in a solution of 0.001 *M* $NiCl_2$ and 0.1 *M* NaCl at pH 5.2. Samples for profiling were taken after 26 h and 45 min, 66 h and 35 min, 120 h, and 168 h. These profiles are seen in Figs. 13–16.

Figure 12 shows the pH profiles expected at each sample time. Time zero corresponds to the 120 h of acid pretreatment and represents the initial pH profile before nickel impregnation. Near the exterior of the pellet, only the effects of the acid diffus-

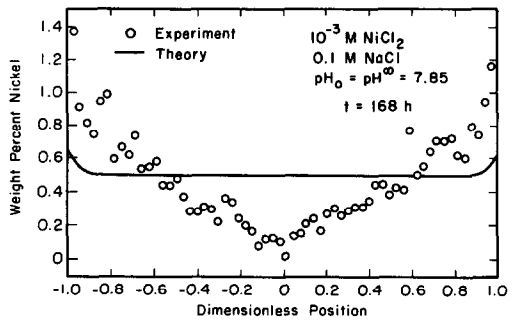

FIG. 11. Nickel profile in a γ-alumina pellet after 168 h. Conditions and parameters are those of Fig. 8.

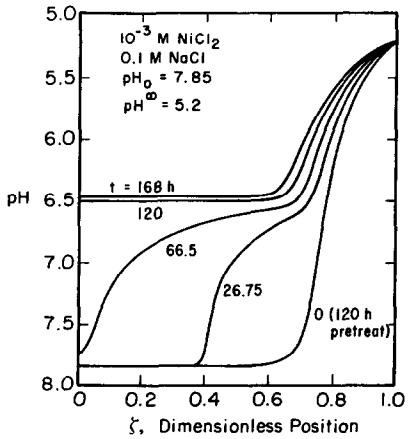

FIG. 12. Calculated pH profiles in a γ-alumina pellet. Initially the pellet is at a uniform pH of 7.85, and then is acid pretreated for 120 h at pH 5.2. Subsequently, the pellet is immersed in a pH 5.2 bath containing 10^{-3} *M* nickel. Requisite parameters are $\Gamma_{1,max}$ (pH = 5.2, $[Ni^{2+}] = 0.0) = 1.49 \times 10^{-10}$ mol/cm², $\Gamma_{2,max}$ (pH 7.85, $[Ni^{2+}] = 10^{-3}$ *M*) $= 3.08 \times 10^{-10}$ mol/cm², $\tilde{D}_1 = 0.20$, $\tilde{D}_2 = 2.6 \times 10^{-2}$, $K = 4.08 \times 10^{-4}$, $\alpha = 69.2$, $\beta = 1.08 \times 10^3$, $\gamma = -9.91 \times 10^{-2}$.

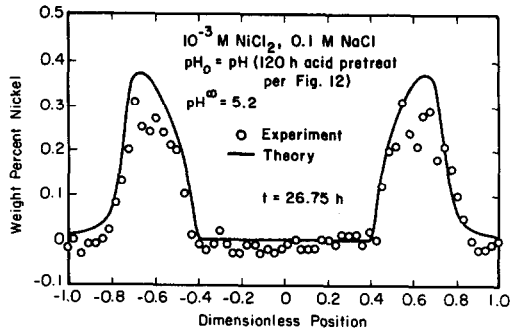

FIG. 13. Nickel profile in a γ-alumina pellet after 26.75 h. Conditions and parameters are those of Fig. 12.

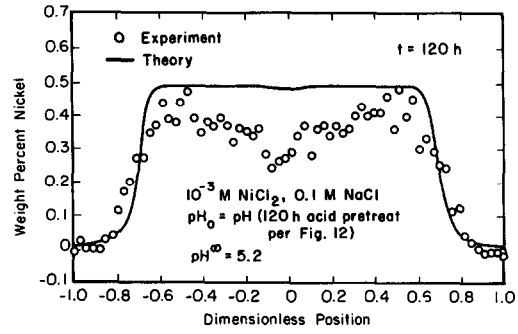

FIG. 15. Nickel profile in a γ-alumina pellet after 120 h. Conditions and parameters are those of Fig. 12.

ing into the pellet are seen. Nickel adsorbs very little in this region of low pH. The interior of the pellet is at a higher pH so the nickel adsorbs strongly in this region, generating excess protons and causing the local pH to decrease from 7.85 to 6.5. After 168 h, the nickel is predicted to reach the center of the pellet, where its pore concentration is essentially the same as the bulk concentration. The nickel profile changes very slowly after it has reached this state because of the slow movement of the excess H^+ ions. Thus, again a pseudo-steady state emerges.

Figure 13 shows the microprobe data and the theoretical profile of nickel for a pellet from the first sample at 26.75 h. As predicted, the nickel diffuses past the outer region of lower pH where adsorption is insignificant. As it reaches the interior of higher pH, it begins to adsorb, forming a band of nickel and creating an egg-white type of catalyst. In the 66.5-h sample shown in Fig. 14, the nickel has moved farther in, and the peaks have almost merged. Figures 15 and 16 show the third and fourth samples at 120 and 168 h, respectively. The nickel has now reached the center of the pellet to create an egg-yolk catalyst. Theory and experimental data on the location of the nickel profiles match well, including confirmation of the slowly emerging pseudo-steady state. The experiments do show a marginally lower nickel content than predicted.

To move the nickel band in an egg-white catalyst closer to the pellet exterior, the length of time for the acid pretreatment should be decreased. In the next experiment, the same procedure as above was followed, except the pellets were immersed in

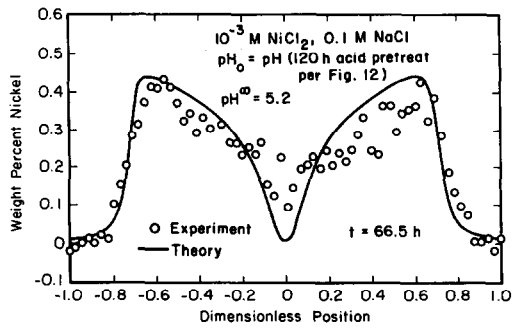

FIG. 14. Nickel profile in a γ-alumina pellet after 66.5 h. Conditions and parameters are those of Fig. 12.

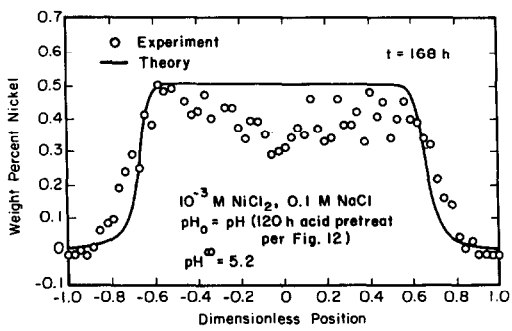

FIG. 16. Nickel profile in a γ-alumina pellet after 168 h. Conditions and parameters are those of Fig. 12.

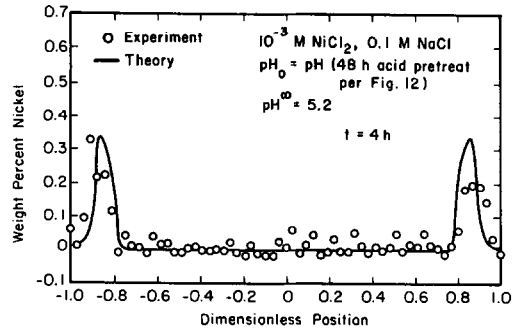

FIG. 17. Nickel profile in a γ-alumina pellet after 4 h. Initially the pellet has a uniform pH of 7.85, and then is acid pretreated for 48 h at pH 5.2. Subsequently, the pellet is immersed in a pH 5.2 bath containing 10^{-3} *M* nickel. Parameters are those of Fig. 12.

the acid impregnation solution for 48 h instead of 5 days. The nickel impregnating solution was the same as in the previous experiment.

Figures 17 and 18 show in turn the experimental and theoretical profiles of samples collected after 4 and 15.67 h. The band of nickel is now located just underneath the exterior surface of the pellet. The position and width of the band have been correctly predicted for both samples, but again the measured amount of nickel is slightly lower than expected. Several more experimental profiles along with comparison to the theoretical predictions may be found in Chu's thesis (*21*).

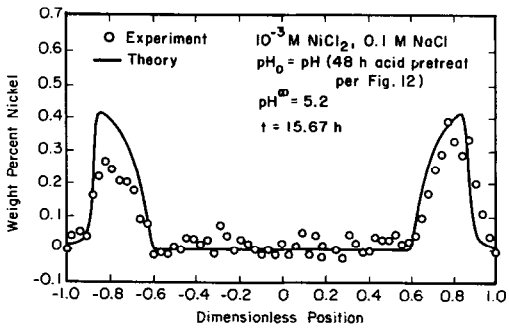

FIG. 18. Nickel profile in a γ-alumina pellet after 15.67 h. Conditions and parameters are those of Fig. 17.

It is clear that judicious choice of acid pretreatment can control metal profiling during wet impregnation of oxide supports. This is because of the dominant role of H^+ and OH^- ions hydrolyzing the surface hydroxyl groups. Further, our proposed transport model correctly reflects the underlying phenomena, thus providing a reliable tool for designing catalyst profiles.

DISCUSSION

We learn from Figs. 8–11 and 13–18 that although the proposed transport model correctly predicts the shape of the metal profiles, it somewhat overpredicts the total amount of nickel present. The total nickel content was calculated for each of the samples by integrating the experimental and the theoretical profiles (*21*). These overall mass ratios range from about 0.6 early in the impregnation process to a little over unity later, near the approach to the pseudo-steady state. This consistent trend of the model overprediction of nickel early to underprediction later suggests that a single phenomenon is causing the same effect in each experiment.

An important assumption made in solving the transport equations is that the background electrolyte concentration remains constant and that the concentrations of HCl and $NiCl_2$ are dilute in comparison. However, as nickel migrates into the pellet, the local pH falls and, accordingly, the adsorption of Na^+ and Cl^- changes. As the pH decreases, more H^+ ions adsorb, and therefore, more Cl^- ions adsorb to form the surface complex $SOH_2^+Cl^-$. In the transport model it is tacitly assumed that this adsorption of Cl^- does not increase enough to change the concentration of chloride in the pores. However, several sample calculations show that this is not generally true (*21*). Even though the surface complex $SOH_2^+Cl^-$ may occupy a small percent of the total number of surface sites, the surface area-to-volume ratio for γ-alumina is so large that the 0.1 *M* chloride concentra-

tion in the pore solution does decrease substantially. Thus Cl^- ions must diffuse in from the bulk solution. Further, from Lewnard's equilibrium studies (*12*), the adsorption isotherms of $NiCl_2$ and HCl show that as the concentration of NaCl decreases, the adsorption of acid and nickel decreases. This is the likely explanation for why in many of the samples, the experimental data at early times show less nickel adsorbed than the model predicts. Later in the impregnation process there is sufficient time for the chloride ions in the pellet to equilibrate with the bulk solution, and the nickel content of the pellet rises close to the model assessments.

The decrease in NaCl pore concentration is also important in the acid pretreatments. In the pH profile calculations, a higher value of D_{H^+}, 2.7×10^{-4} cm^2/s, as compared to the literature value of 9.3×10^{-5} cm^2/s (15), was used to increase the rate of acid penetration and to predict more accurately the location of the nickel band in the egg-white catalysts. Since a decrease in NaCl concentration results in a lower Γ_{HCl}, the acid penetrates farther than expected, and the value of D_{H^+} could be lowered to approach the literature value. All of our experimental results are consistent with the hypothesis that the NaCl pore concentration has decreased from the bulk concentration (*21*). The depletion of NaCl from the pore solution explains both the small experimental amounts of nickel initially present and the consistent trend of increasing nickel content ratios later during impregnation.

To quantify the diffusion behavior of NaCl, five additional equations would have to be added to the present model: two transport equations for Na^+ and Cl^-, two equations defining the adsorption of Na^+ and Cl^-, and a charge balance to maintain electroneutrality in the pore solution. The electrical migration terms would also have to be included in all transport equations. We have not pursued this more rigorous calculation.

CONCLUSIONS

A transient transport model has been developed that provides physical insight into the surface chemistry of ion adsorption from aqueous solution on oxides and diffusion into a porous solid. Wet impregnation of nickel in a γ-alumina catalyst pellet is successfully simulated. Since adsorption of nickel on γ-alumina is strongly influenced by pH, highly coupled and nonlinear diffusion equations are demanded for acid and for nickel. A realistic, triple-layer electrostatic description of the adsorption of Ni^{2+} ions, background electrolyte ions, and H^+ and OH^- ions is paramount. The crucial ion-exchange behavior is the generation of protons as nickel adsorbs. This behavior cannot be predicted by a simple Langmuir model, yet it is essential for quantifying the unique, concave–convex metal profiles observed experimentally.

New electron-microprobe metal profiles on γ-alumina have been obtained with a system of $NiCl_2$, HCl, and 0.1 *M* NaCl as the background electrolyte, over a nickel concentration range of 0.001 to 0.1 *M*, and a pH range from 5.2 to 7.85. The resulting catalysts had nickel loadings ranging from zero to 7.5 wt%. Several experimental profiles from each sample indicate that the data are highly reproducible; all of the measured profiles are radially symmetric. Catalysts with a uniform profile with increased loading near the exterior were produced (*21*), as well as egg-yolk, egg-white, and egg-shell catalysts. Modifying the acid pretreatment conditions clearly demonstrates how the band of nickel in an egg-white catalyst can be controlled.

All parameters underlying the theoretical diffusion calculations were obtained a priori, except for a relatively minor adjustment in the hydrogen ion diffusion coefficient. When viewed in this manner, agreement between theoretical and experimental impregnation profiles is very good. The observed discrepancies are most likely explained by a lack of constant pore concen-

tration of the background electrolyte due to surface complexing with acid hydrolyzed sites. The proposed transport model provides an important, new tool for designing metal profiles of oxide catalyst supports.

APPENDIX A: EQUILIBRIUM ADSORPTION MODEL

Davis, James, and Leckie have developed a triple-layer electrostatic model for the oxide surface/aqueous solution interface (*11*). As shown in Fig. 2 there are three planes of interest. At the innermost plane, the o-plane, only H^+ and OH^- ions are adsorbed. They contribute to the surface charge of the o-plane, σ_o, and experience the potential at that plane, ψ_o. Na^+ and Cl^-, the background electrolyte ions, are partially hydrated and complex at the β-plane with oppositely charged surface groups. Ni^{2+} ions are also specifically adsorbed at the β-plane as partially hydrated cations binding with deprotonated surface sites (*12*). Na^+, Cl^-, and Ni^{2+} all contribute to the surface charge of the β-plane, σ_β, and experience the potential at that plane, ψ_β. The outermost plane, the beginning of the diffuse region, is composed of all fully hydrated coions and counterions in solution. This diffuse layer has a corresponding potential, ψ_d, and charge, σ_d. The o-plane and the β-plane are separated by a region of integral capacitance Ω_1, and the β-plane and the diffuse plane are separated by a region of integral capacitance Ω_2.

Adsorption of specific ions may be described as simple ionization and binding reactions of the surface acid or base groups. Local equilibrium reactions with corresponding equilibrium constants can be written for each ion:

$$\mathrm{SOH} + \mathrm{H^+} \overset{K_1}{\rightleftarrows} \mathrm{SOH_2^+} \qquad \text{(A1)}$$

$$\mathrm{SOH} \overset{K_2}{\rightleftarrows} \mathrm{SO^-} + \mathrm{H^+} \qquad \text{(A2)}$$

$$\mathrm{SOH} + \mathrm{H^+} + \mathrm{Cl^-} \overset{K_3}{\rightleftarrows} \mathrm{SOH_2^+Cl^-} \qquad \text{(A3)}$$

$$\mathrm{SOH} + \mathrm{Na^+} \overset{K_4}{\rightleftarrows} \mathrm{SO^-Na^+} + \mathrm{H^+} \qquad \text{(A4)}$$

$$\mathrm{SOH} + \mathrm{Ni^{2+}} + \mathrm{H_2O} \overset{K_{Ni}}{\rightleftarrows} \mathrm{SO^-NiOH^+} + 2\mathrm{H^+}. \qquad \text{(A5)}$$

SOH represents a hydroxylated surface site. Let $\Psi_i = \psi_i F/RT$ be the nondimensionalized electrostatic potential at plane i. Mass-action equations including an electrostatic correction can now be written for each surface species in terms of bulk concentrations and the three different potentials (*11, 12*):

$$\{\mathrm{SOH_2^+}\} = K_1\{\mathrm{SOH}\}[\mathrm{H^+}]\exp(-\Psi_o), \qquad \text{(A6)}$$

$$\{\mathrm{SO^-}\} = \frac{K_2\{\mathrm{SOH}\}}{[\mathrm{H^+}]\exp(-\Psi_o)}, \qquad \text{(A7)}$$

$$\{\mathrm{SOH_2^+Cl^-}\} = K_3\{\mathrm{SOH}\}[\mathrm{H^+}][\mathrm{Cl^-}]\exp(-\Psi_o)\exp(+\Psi_\beta), \qquad \text{(A8)}$$

$$\{\mathrm{SO^-Na^+}\} = \frac{K_4\{\mathrm{SOH}\}[\mathrm{Na^+}]\exp(-\Psi_\beta)}{[\mathrm{H^+}]\exp(-\Psi_o)}, \qquad \text{(A9)}$$

$$\{\mathrm{SO^-NiOH^+}\} = \frac{K_{Ni}\{\mathrm{SOH}\}[\mathrm{Ni^{2+}}]\exp(-\Psi_\beta)}{[\mathrm{H^+}]^2\exp(-\Psi_o)}. \qquad \text{(A10)}$$

The braces { } denote surface concentrations of the reaction complexes and the brackets [ ] denote bulk solution concentrations.

As acid and base surface groups selectively ionize and unequal amounts of cations and anions are adsorbed, the surface develops a charge. This surface charge is distributed among that at the o-plane, the β-plane, and the diffuse region such that electroneutrality is obeyed:

$$\sigma_o + \sigma_\beta + \sigma_d = 0. \qquad \text{(A11)}$$

Charge–potential relationships, or Gauss' law, must also be obeyed for both of the constant capacitance regions. These principles along with the definitions of the surface charges at each plane in terms of the various ion complexes demand the following electrostatic constraints at each plane.

We write for the o-plane,

$$\sigma_o = F[\{SOH_2^+\} - \{SO^-\} - \{SO^-NiOH^+\}] = \Omega_1[\psi_o - \psi_\beta], \quad (A12)$$

for the β-plane,

$$\sigma_\beta = F[\{SO^-Na^+\} - \{SOH_2^+Cl^-\} + \{SO^-NiOH^+\}] = \Omega_1[\psi_\beta - \psi_o] + \Omega_2[\psi_\beta - \psi_d], \quad (A13)$$

and for the d-plane,

$$\sigma_d = [2\varepsilon R_g T/(\lambda F)] \sinh[\Psi_d/2] = \Omega_2[\psi_\beta - \psi_d], \quad (A14)$$

where λ is the Debye length (*11, 15*). Additionally, site conservation demands that the total number of hydrolyzable groups per unit surface area, S_t, be distributed among all ion-complexed states:

$$S_t = \{SOH\} + \{SOH_2^+\} + \{SO^-\} + \{SOH_2^+Cl^-\} + \{SO^-Na^+\} + \{SO^-NiOH^+\}. \quad (A15)$$

With bulk concentrations and the total site density known, Eqs. (A6)–(A10) and (A12)–(A15) constitute a set of 12 equations in 12 unknowns. To effect a solution we adopt the general, numerical scheme of Westall for electrostatic adsorption models (*13*). With the particular DJL (*11*) equilibrium formulation, calculation of the following variables is recommended by Westall: the dimensionless concentration of empty surface sites, $\{SOH\}/S_t$, the dimensionless o-plane potential, Ψ_o, the dimensionless β-plane potential, Ψ_β, and the dimensionless diffuse plane potential, Ψ_d. These four unknowns are established by solving the right pair of Eqs. (A12)–(A14) and (A15). All other variables are eliminated using the remaining independent equations. A Newton–Raphson iteration scheme is applied in the four unknowns. Although an initial guess is required, the method converges over a fairly wide range of guesses (*21*).

Once convergence is achieved, adsorption of the components may be calculated by accounting for all molecular states of the acid and nickel species:

$$\Gamma_{HCl} = \Gamma_{H^+} - \Gamma_{OH^-} = \{SOH_2^+\} + \{SOH_2^+Cl^-\} + \Gamma(H^+)_d - \{SO^-\} - \{SO^-Na^+\} - 2\{SO^-NiOH^+\} - \Gamma(OH^-)_d, \quad (A16)$$

$$\Gamma_{NiCl_2} = \Gamma_{Ni^{2+}} = \{SO^-NiOH^+\} + \Gamma(Ni^{2+})_d, \quad (A17)$$

$\Gamma(i)_d$, the Gibbsian adsorption of species i in the diffuse region, is defined as (15)

$$\Gamma(i)_d = 2\,|z_i|\,C_i\lambda\,[\exp(-z_i\Psi_d/2) - 1]. \quad (A18)$$

Note that the adsorption of HCl accounts for the two protons released for every nickel ion adsorbed. To calculate HCl adsorption without nickel present, the nickel surface species is omitted from Eqs. (A12)–(A16).

The extensive adsorption uptake measurements of Lewnard for γ-alumina (*12*) permit fitting of the various ion-binding constants and the integral capacitances. Their values are $K_1 = 1.8 \times 10^8$ m^3/kmol, $K_2 = 2.1 \times 10^{-8}$ kmol/m^3, $K_3 = 4.4 \times 10^6$ (m^3/kmol)^2, $K_4 = 1.1 \times 10^{-9}$ dimensionless, $K_{Ni} = 3.2 \times 10^{-12}$ m^3/kmol, $\Omega_1 = 220$ μF/cm^2, and $\Omega_2 = 20$ μF/cm^2. Independent tritium uptake fixes the total site density at $S_t = 3.12 \times 10^{-9}$ mol/cm^2 (*12*).

During the transient diffusion calculations, the equilibrium relations, Eqs. (A6)–(A10) and (A12)–(A17), are solved simultaneously along with the diffusion equations to yield pellet profiles in $\{SOH\}/S_t$ and Ψ_i in addition to the metal and acid concentration and adsorption profiles (*21*). The concentration of NaCl is fixed at the bulk solution value according to the supporting electrolyte assumption.

APPENDIX B: NOTATION

A_v Surface-to-volume ratio, m^2/m^3
C_i Concentration of species i, kmol/m^3
$\tilde{C}_i$ Nondimensional concentration of component i

D_i Diffusion coefficient of species i, m²/s
$\tilde{D}_1$ Ratio of D_{H^+}/D_{OH^-}
$\tilde{D}_2$ Ratio of $D_{M^{2+}}/D_{H^+}$
F Faraday's constant, C/mol
K $\equiv 2K_w/(C^{\infty}_{10} - C^{\circ}_{10})^2$, dimensionless water dissociation constant
K_i Ion-binding equilibrium constant for surface species i, units depend on particular reaction.
K_w Equilibrium constant for dissociation of water, (kmol/m³)²
r Radial distance, m
R Radius of cylindrical pellet, m
R_g Ideal gas constant, J/mol/K
S_t Total concentration of surface hydrolyzable groups, kmol/m²
T Temperature, K
t Time, s
z_i Valence of species i
α Dimensionless isotherm chord ratio, defined in Eq. (17)
β Dimensionless gauge of metal adsorption and pore solution concentrations, defined in Eq. (18)
γ $\equiv C^{\circ}_{10}/C^{\infty}_{10} - C^{\circ}_{10})$, ratio of initial acid concentration at pellet center to that at exterior bulk solution
Γ_i Adsorption of species i, kmol/m²
$\tilde{\Gamma}_i$ Nondimensional adsorption of species i
ε Liquid solution permittivity, C/V · m
ζ Nondimensional radial distance
θ Tortuosity
τ Nondimensional time, defined in Eq. (14)
λ Debye length, m
σ_i Charge at surface plane i, C/m²
ϕ Porosity
ψ_i Electrostatic potential at surface i, V
Ψ_i Dimensionless electrostatic potential at surface i
Ω_i Integral capacitance in region i, F/m²
∞ Superscript, bulk solution property
$\circ$ superscript, pellet center
0 Subscript, initial condition
d Subscript, diffuse region
s Subscript, pseudo-steady state
{ } Surface species concentration, kmol/m²
[ ] bulk solution species concentration, kmol/m³

ACKNOWLEDGMENTS

This work was partially supported by the National Science Foundation under Grant NSF 83-14564. We thank the Department of Geology of the University of California at Berkeley for access to the wavelength-dispersive electron microprobe and for the help of John Donovan and Tim Teague in obtaining the profile analyses.

REFERENCES

1. Komiyama, M., *Catal. Rev. Sci. Eng.* **27,** 341–372 (1985).
2. Lee, S. Y., and Rutherford, A., *Catal. Rev. Sci. Eng.* **27,** 207–340 (1985).
3. Dougherty, R. C., and Verykios, X. E., *Catal. Rev. Sci. Eng.* **29**(1), 101–150 (1987).
4. Komiyama, M., and Merrill, R. P., *Bull. Chem. Soc. Japan* **57,** 1169–1173 (1984).
5. Shyr, Y. S., and Ernst, W. R., *J. Catal.* **63,** 425–432 (1980).
6. Chen, H. C., and Anderson, R. B., *J. Catal.* **43,** 200–206 (1976).
7. Vincent, R. C., and Merrill, R. P., *J. Catal.* **35,** 206–217 (1974).
8. Kulkarni, S. S., Mauze, G. R., and Schwarz, J. A., *J. Catal.* **69,** 445–453 (1981).
9. Hegedus, L. L., Chou, T. S., Summers, J. C., and Potter, N. M., "Multicomponent Chromatographic Processes during the Impregnation of Alumina Pellets with Noble Metals" (B. Delmon, P. Grange, P. Jacobs, and G. Poncelot, Eds.), Preparation of Catalysts II, pp. 171–184. Elsevier, Amsterdam, 1979.
10. Komiyama, M., Merrill, R. P., and Harnsberger, H. F., *J. Catal.* **63,** 35–52 (1980).
11. Davis, J. A., James, R. O., and Leckie, J. O., *J. Colloid Interface Sci.* **63** (3), 480–499 (1978).
12. Lewnard, J., "Ionic Adsorption and Diffusion in Porous Metal Oxides," Ph.D. thesis, University of California, Berkeley, 1985.
13. Westall, J., "Chemical Equilibria Including Adsorption of Charged Surfaces," Advances in Chemistry Series No. 189, pp. 33–44, American Chemical Society, Washington, D.C. 1980.
14. Lewnard, J. J., Petersen, E. E., and Radke, C. J., *J. Chem. Soc. Faraday Trans. 1* **84**(*11*), 3927–3939 (1988).
15. Newman, J. S., "Electrochemical Systems." Prentice-Hall, Englewood Cliffs, NJ, 1973.
16. Helfferich, F., "Ion Exchange." McGraw-Hill, New York, 1962.
17. Helfferich, F., *J. Phys. Chem.* **69,** 1178–1185 (1965).

18. Holl, W., and Sontheimer, H., *Chem. Eng. Sci.* **32,** 755–762 (1977).

19. Kataoka, T., and Yoshida, H., *Canad. J. Chem. Eng.* **59,** 475–482 (1981).

20. Tsai, T. T., "Adsorption–Desorption Kinetics during the Impregnation of an Alumina Support by Aqueous Nickel Chloride Solutions." M.S. thesis, University of California, Berkeley, 1982.

21. Chu, P., "Metal Ion Diffusion in Porous Oxides with Surface Complexation." M.S. thesis, University of California, Berkeley, 1987.

22. Satterfield, C. N., "Heterogeneous Catalysis in Practice." McGraw–Hill, New York, 1980.

23. Purdy, G. R., and Anderson, R. B., "Experimental Methods in Catalytic Research" (R. B. Anderson and P. T. Dawson, Eds.), Vol. II. Academic Press, New York, 1976.

24. Fitzgerald, R., "Electron Microprobe Instrumentation: Microprobe Analysis" (C. A. Andersen, Ed.), pp. 3–51. John Wiley, New York, 1973.